Soft Matter

Glass transition of ion-containing polymer melts in bulk and thin films

Journal:	*Soft Matter*
Manuscript ID	SM-ART-07-2021-001098.R1
Article Type:	Paper
Date Submitted by the Author:	27-Aug-2021
Complete List of Authors:	Li, Wei; University of Tennessee Knoxville College of Engineering, Chemical and Biomolecular Engineering Olvera de la Cruz, Monica; Northwestern University, Materials Science and Engineering

Glass transition of ion-containing polymer melts in bulk and thin films

Wei Li[†] and Monica Olvera de la Cruz[*,†,‡,¶,§]

†*Department of Materials Science and Engineering, Northwestern University, Evanston, IL 60208*

‡*Department of Physics and Astronomy, Northwestern University, Evanston, IL 60208*

¶*Department of Chemistry, Northwestern University, Evanston, IL 60208*

§*Department of Chemical and Biological Engineering, Northwestern University, Evanston, IL 60208*

E-mail: m-olvera@northwestern.edu

Abstract

Ion-containing polymers often are good glass former, and the glass transition temperature is an important parameter to consider for practical applications, which prescribes the working temperature range for different mechanical and dynamic properties. In this work, we present a systematic molecular dynamics simulation study about the coupling of ionic correlations with the glass transition, based on a generic coarse-grained model of ionic polymers. The variation of glass transition temperature is examined concerning the influence of electrostatic interaction strength, charge fraction, and charge sequence. The interplay with the film thickness effect is also discussed. Our results reveal a few typical features about the glass transition process that are in qualitative agreement with previous studies, further highlighting the effects of counterion entropy at weak ionic correlations and physical crosslinking of ionic aggregates at strong ionic correlations. Detailed parametric dependencies are displayed, which demonstrate that

introducing strong ionic correlations promotes vitrification while adopting a precise charge sequence and applying strong confinement with weak surface affinity reduce the glass transition temperature. Overall, our investigation provides an improved picture towards a comprehensive understanding of the glass transition in ion-containing polymeric systems from a molecular simulation perspective.

Introduction

Ion-containing polymers, such as ionenes,[1,2] ionomers,[3–5] polyelectrolytes,[6,7] and polymerized ionic liquids,[8,9] have long been used in commercial products,[10] while gaining increasing attention in recent years for emerging applications in catalyst layers,[11] shape-memory materials,[12] gas separation membranes,[13,14] drug delivery,[15] antimicrobial materials,[16] and energy storage and conversion,[17] etc. Incorporating ionic functional groups into polymers, either within the backbone or bonded as pendants, can significantly enhance the thermal and mechanical properties of associating polymeric materials. The structure motifs formed by ionic aggregates, functioning as physical crosslinks that improve strength, toughness, and modulus, generate tough thermoplastic elastomers and high-performance polymers which exhibit shape memory and self-healing properties.[10] Moreover, ionic polymers, with one type of charge species covalently attached to the polymer chain with low mobility, have high transference numbers (near unity)[7,17] and when used as solid electrolytes in the battery, can prevent the formation of a concentration gradient between electrodes from charge-discharge cycles.[18] These features make ionic polymers, especially polymerized ionic liquids (having weak electrostatic interactions between ion pairs and high ion conductivity), desirable materials for single-ion conductors that are critical for next-generation energy technologies.[17,18]

Significant progress has been made over the past decade in enhancing the performance of ionic polymers in a range of applications.[2,10] Nevertheless, effective design principles are still needed for performance optimization, for which developing relevant structure-property relationships is of fundamental importance. Herein, we focus on one key physical prop-

erty, namely, glass transition. Polymers are generally good glass formers and are commonly present in the glassy state, which undergo drastic changes in mechanical and dynamic properties over a small range of temperature around the glass transition temperature, T_g.[19–21] Consequently, T_g dictates the working temperature range of polymers for desired properties and hence, is a crucial parameter to consider in designing polymeric materials. For instance, ionic polymers, when possessing high T_g, appear to have relatively lower polymer mobility and ion conductivity at room temperature.[18] In this regard, lowering the polymer T_g offers a tractable handle to increase ion transport and conductivity, which improves the performance of polymer electrolytes.[17,22]

Due to its important practical relevance, studying T_g of polymers, both in bulk and in confinements, is of considerable interest.[21,23] Alongside experimental investigations and theoretical developments,[24–27] computer simulations provide indispensable molecular level information that aids in the understanding of polymer glass transition in addition to phenomenological pictures.[19,28–31] Particularly, molecular dynamics simulations based on generic coarse-grained (CG) models,[28,32] being computationally efficient, offer a powerful tool to interrogate the effects of ionic correlations on ionic aggregates and ion transport properties,[33–43] as well as the influence on glass transition and vitrification kinetics,[44–47] in ionic polymers.

Ruan and Simmons[45,46] employed a CG model of ionomers, each containing 20 neutral beads and a single ionic group (bonded in the middle or at one end of the ionomer), and studied the polymer dynamics around separate ionic aggregates based on the relaxation time extracted from incoherent intermediate scattering function. They found that T_g is increased for polymer segments close to 'rigid' ionic aggregates (under strong electrostatic interactions with the dielectric constant of $\varepsilon_r = 4$), indicating the suppression of local segmental dynamics induced by steric constraints.[45] This, in turn, increases the system T_g. From comparing systems of different polymer chain bending energies, they demonstrated that increasing the chain stiffness also increases T_g, while the dynamic suppression near ionic aggregates is relatively smaller at larger stiffness. Moreover, they suggested that the size of reduced-

mobility regions around ionic aggregates is correlated with the scale of segmental cooperative motion instead of chain persistence length.[46] Fu et al.[47] studied the glass transition for a model of precise ionenes with a charge fraction of 0.25 and contrasted systems of different counterion sizes at $\varepsilon_r = 10$ and 30 for flexible and semi-flexible chains. They showed that T_g exhibits a non-monotonic behavior with varying the counterion size, while $\varepsilon_r = 10$ and semi-flexible chains lead to comparatively higher T_g. Despite that a couple of simulation studies have shown specific features about the glass transition of ionic polymers, the related control parameter space remains largely unexplored. We attempt to address this need by using systematic molecular dynamics simulations.

In the present study, we explore the influence of ionic correlations on the glass transition of ionic polymers, both in bulk and in confined thin films. We adopted a simplified coarse-grained model to depict typical characters of ionic polymers, which assumes a uniform relative permittivity and the same particle size of CG beads for simplicity. The glass transition process was probed via isobaric annealing (with a constant cooling rate) using molecular dynamics simulations. And T_g was determined following a pseudo-thermodynamic approach through dilatometric measures.[47,48] From comparing T_g in different control groups, we examine the effects of electrostatic interaction strength, charge fraction, and charge sequence on the glass transition in bulk. A detailed dependence of T_g on the associated ionic correlations is exposed, along with the analysis of configurational and dynamical properties which presents the coupling of ionic associations with polymer relaxation and ion transport. We also probe the glass transition of ionic polymers in thin films confined by smooth walls (having a weak surface affinity to particles), with a focus on the effect of film thickness h. A general trend in the decrease of T_g with decreasing h is revealed, highlighting the contribution of surface layers with a relatively lower particle density and higher mobility compared to the bulk-like layer. Its interplay with interfacial interactions and ionic correlations is further discussed. In general, our investigation demonstrates a few characteristic features about the glass transition in ion-containing polymeric systems, providing molecular insight

into tailoring T_g for the rational design of ionic polymer materials.

Model Systems and Simulation Method

We exploited a generic coarse-grained model to study the glass transition of ionic polymers.[34–36,41,43] For simplicity, we adopted linear polymers with charge species embedded within the chain backbone. We note that the polymer architecture affects chain packing and segmental dynamics, which alters T_g.[49] Meanwhile, the architecture difference between ionomer and ionene can cause different structures of ionic aggregates (e.g., compact discrete aggregates versus extended aggregates[34]), as well as different ion transport properties.[36,37] Nevertheless, we expect that the qualitative behaviors exposed based on the simplified model should have general implications for understanding the effects of ionic correlations on the glass transition.

Standard Lennard–Jones (LJ) reduced units were adopted. The ionic polymer was depicted by a bead-spring chain,[50] which consisted of neutral (na) and charged (ca) beads (Figure 1a). The neighboring beads along the chain backbone were bonded via a finitely extensible nonlinear elastic (FENE) potential, $U_{\mathrm{FENE}}(r) = -0.5k_bR_0^2\ln(1 - r^2/R_0^2)$, with a spring constant $k_b = 30\epsilon/\sigma^2$ and a maximum length of $R_0 = 1.5\sigma$ to avoid chain breaking or unphysical crossing.[50] Each ca bead carried an elementary charge of $q = e/\sqrt{4\pi\varepsilon_0\sigma\epsilon}$ (e is the elementary charge in coulomb units and ε_0 is the vacuum permittivity). The pairing counterion (ci) had an opposite charge, $-q$. The simulation box contained equal amounts of ca and ci and was charge neutral in total. The charge fraction of the system was defined as $f_c = n_{ca}/(n_{na} + n_{ca})$, where n_i is the total number of type i particles. All particles were of unit mass m and diameter σ. Besides electrostatic interactions between charged particles, the pairwise interaction was dictated by a LJ potential, $U_{\mathrm{LJ}}(r) = 4\epsilon_{LJ}[(\sigma/r)^{12} - (\sigma/r)^6]$ for $r < r_c$, with an energy coefficient of $\epsilon_{LJ} = 1.0\epsilon$ and interaction cutoff at $r_c = 2.5\sigma$ (potential shift was applied to let $U_{\mathrm{LJ}}(r_c) = 0$).

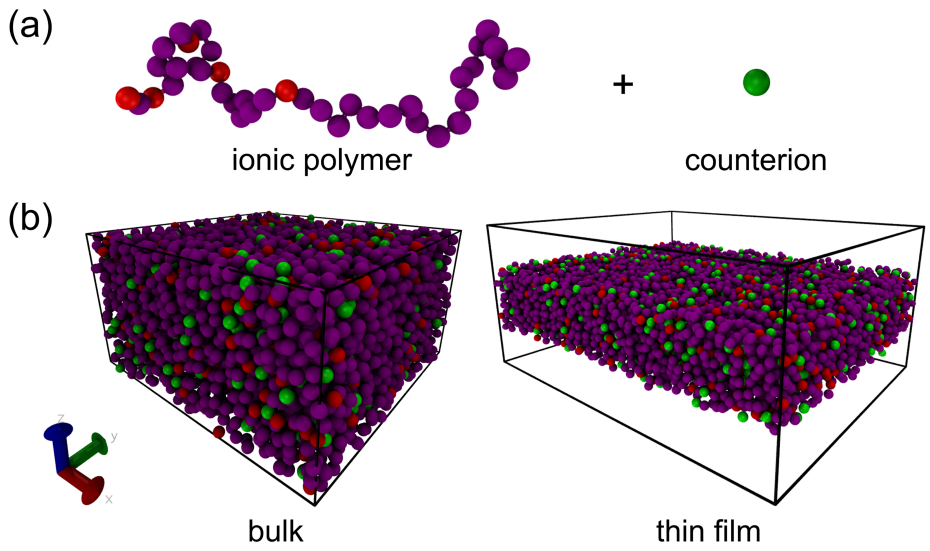

Figure 1: (a) Model system contains ionic polymers and counterions, which is charge neutral in total. The ionic polymer is depicted by a bead-spring model, consisting of neutral (na) and charged (ca) beads (colored in purple and red, respectively), where ca is treated the same as na but carries an elementary charge, q. The counterion (ci, colored in green) has an opposite charge, $-q$. In the illustration, ca beads are randomly distributed along the chain. (b) Simulation setup for bulk and thin film systems, containing 160 and 272 ionic polymers, respectively.

In this study, each ionic polymer comprises $N = 40$ beads. Noticing that the neutral polymer glass transition temperature $T_g \sim 1/N$ according to the Fox–Flory equation and it shows saturation at $N = 40$ for flexible chains (as well as no manifest dependence on the chain length polydispersity),[51] one would expect that a further increase in N may not significantly affect T_g, since the glass transition is not sensitive to chain dynamics while the relative chain end effect decreases with increasing N. For the parameter mapping to real units of the modeling, we selected $\sigma = 1.0\,\mathrm{nm}$ and $\epsilon = 1k_\mathrm{B}T^*$ (k_B is the Boltzmann constant), with the reference temperature $T^* = 298\,\mathrm{K}$ that corresponds to the reduced LJ temperature $T = 1.0$. Accordingly, $q = 7.4853$. All quantities were made dimensionless with respect to length unit σ, energy unit ϵ, mass unit m, and time unit $\tau = \sigma(m/\epsilon)^{1/2}$.

We considered both bulk and thin film systems (Figure 1b). A uniform dielectric constant, ε_r, was assumed for the systems, which was tuned to control the strength of electrostatic interactions in simulations. The electrostatic interaction strength was further characterized

by the Bjerrum length, $l_B = q^2\sigma/\varepsilon_r$, capturing the distance at which the interaction energy between two elementary charges equals $1k_{\mathrm{B}}T^*$ in magnitude. In addition to f_c and l_B, the charge sequence along the chain was also varied to contrast the behaviors of random and precise ionic polymers. Specifically, for the random sequence, ca beads were allocated randomly along the polymer (for which the chain charge number exhibits a Gaussian distribution, see Figure S1 in the Supplementary Information). By contrast, the first bead of every $1/f_c$ beads was assigned as ca in the precise ionic polymer.

The molecular dynamics simulations were performed by using LAMMPS.[52] A standard velocity-Verlet time integrator was employed with a time step of $\delta t = 0.005\tau$. We utilized a Langevin thermostat to control temperature and a Nosé–Hoover barostat to keep the external pressure at $P = 0$ (T_g depends on P), with the damping parameters both of 0.5τ. In the bulk system, periodic boundary conditions were enforced in the simulation box (of size $L_x \times L_y \times L_z$), while the barostat was applied independently in all three directions. The film system was constructed by bounding polymer domain (containing counterions) along the z-direction with flat smooth walls at $z = -h/2$ and $h/2$ (the simulation box edges were located at $\pm L_z/2$ and $L_z > h$), yielding the film thickness of h. The wall exerted a force on particles in the z-direction (perpendicular to the wall) according to the interaction potential, $U_{\mathrm{wall}}(r) = \epsilon_{\mathrm{wall}}[(2/15)(\sigma/r)^9 - (\sigma/r)^3]$, for $r < r_c^w$ (with the potential shifted to 0.0 at r_c^w). If not otherwise specified, $\epsilon_{\mathrm{wall}} = 1.0\epsilon$ and the cutoff distance $r_c^w = 1.1225\sigma$, leading to weakly attractive walls to all the particles (with the attraction well depth of 0.394ϵ). The periodic boundary conditions and independent barostat were applied in the x and y directions. Moreover, the thermostat was turned off along the z-direction to exclude the wall effect. The long-range electrostatic interactions were treated by a particle-particle particle-mesh (PPPM) solver, and a modified version for the slab geometry was used for thin films.[53] Its accuracy for the force error tolerance was set as 10^{-4}, while the cutoff distance for separating calculations in real and reciprocal spaces was optimized for individual systems.

The glass transition was probed by a quenching process. Specifically, the simulation

system was started with a random configuration (in a large box) and first equilibrated at $T = 1.0$ for 1×10^7 time steps (see Figure S2 for an example of the temporal evolution of thermodynamic quantities during the equilibration process), which is sufficient for chain relaxation (cf. Figure S3 for typical end-to-end autocorrelation functions). Taking the final system configuration, a cooling run was performed with T ramped from 1.0 to 0.1 at a constant rate of $\Delta T/\Delta t = -2 \times 10^{-5}\tau^{-1}$ (for 9×10^6 time steps). Noting that T_g depends on the quenching process,[54] the same cooling rate was maintained throughout the investigation for comparisons. System configurations were typically saved at a time interval of 5×10^5 time steps (i.e., $|\Delta T| = 0.05$) and later, used as initial configurations for subsequent relaxation runs of 5×10^6 time steps at corresponding temperatures. Additional 5×10^6 time steps were run for the data collection of thermodynamic quantities. All these procedures were conducted in the NPT ensemble. For dynamic properties, additional runs in the NVT ensemble were carried out after adjusting the simulation cell size to the average value obtained from the NPT production run.

We followed a pseudo-thermodynamic approach and used dilatometric measures to determine T_g (in contrast to dynamic measurements[48,55]). Specifically, the variation of specific volume, $V^* = V/(n_{na} + 2n_{ca})$, along with decreasing T shows a kink around the glass transition, indicating the difference between thermal expansion coefficients of the melt and glass states. Herein, V^* was collected from the production runs at different T and then, plotted as a function of T (see Figure S4 for example, including a comparison with total energy profile from calorimetric measures[48]). Linear fittings were performed in the linear regimes close to the transition on the two sides, where T_g was taken from the intersection between two fitted lines. In particular, we selected common T ranges in different systems to compute T_g for comparison. Statistical data were obtained from averaging results over three independent sets of the same systems.

Results and Discussion

Effect of the ionic correlation strength. In Figure 2a, we plot V^* as a function of T for bulk random ionic polymers of $f_c = 0.1$ at different l_B. Specifically, $l_B = 0$ refers to a neutral system where electrostatic interactions are turned off in simulations that counterions function as neutral solvent particles. With increasing l_B and the strength of electrostatic interactions, V^* decreases, and the reduction is larger at higher temperatures, shifting the kink position towards larger T. We summarize the variation of T_g as a function of l_B in Figure 2b, which exhibits a monotonic increase as l_B increases. Furthermore, the sublinear trend indicates a more complex dependence of T_g on the ionic correlations in contrast to the linear dependence suggested based on an intuitive hypothesis that the thermal energy associated with T_g is proportional to the electrostatic potential energy of a charge pair,[56] i.e., $k_{\mathrm{B}}T_g \propto l_B\varepsilon/\sigma$ that $T_g \propto l_B$.

To discern the influence of electrostatic interactions on the correlation between polymer beads and glass transition, we plot the radial distribution function between neutral beads, $g_{\text{na-na}}(r)$, for systems of different l_B (at $T = 0.7$) in Figure 2c. The primary peak at the separation $r \approx 0.953$ is dictated by the FENE bond between neighboring beads along the chain contour, which is about the same in different systems. The next peak in $g_{\text{na-na}}(r)$ (around $r^* \approx 1.09$) corresponds to the correlation between nearest-neighbor beads, and its height increases with increasing l_B (and decreasing V^*). The same behavior is also found in the other peaks, which is analogous to the effect of increasing ϵ_{LJ} (cf. Figure S5). This suggests that introducing the ionic correlations effectively enhances the overall cohesive energy and hence the correlations among polymer beads.

We select the height of the nearest-neighbor peak, $g_{\text{na-na}}(r^*)$, as an indicator for the polymer pair correlation. Its variation with l_B is presented in Figure 2d, conforming well with the monotonic trend shown in Figure 2b. Such behavior is retained with varying T, while $g_{\text{na-na}}(r^*)$ increases with decreasing T (Figure S6). Moreover, the plot of $g_{\text{na-na}}(r^*)$ at corresponding T_g as a function of l_B also shows a monotonic increase (Figure S6), implying

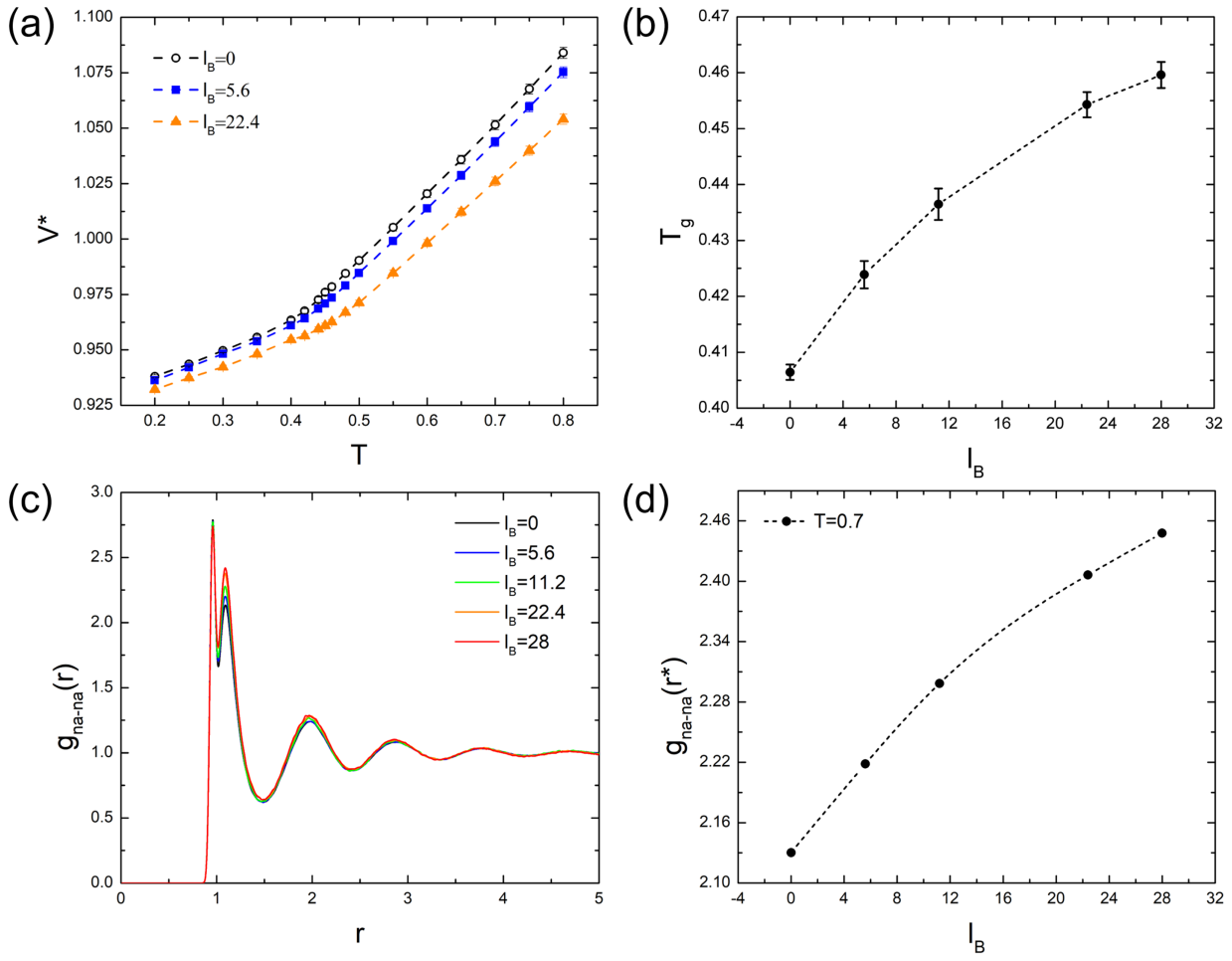

Figure 2: (a) Specific volume, V^*, as a function of temperature T from cooling (with a constant cooling rate $\Delta T/\Delta t = -2 \times 10^{-5}\tau^{-1}$) for bulk random ionic polymers of charge fraction $f_c = 0.1$ at different values of Bjerrum length l_B, where $l_B = 0$ corresponds to the neutral system without electrostatic interactions. (b) Glass transition temperature, T_g, as a function of l_B. (c) Radial distribution function between neutral beads, $g_{\text{na-na}}(r)$, in systems of $T = 0.7$ at different l_B. (d) Corresponding height of the nearest-neighbor peak, $g_{\text{na-na}}(r^*)$, as a function of l_B.

that the glass transition takes place at a higher temperature and larger effective polymer correlation with increasing the electrostatic interaction strength.

Next, we examine polymer dynamic properties to expose general features of the glass transition, using the system of $f_c = 0.1$ and $l_B = 5.6$ with $T_g \approx 0.424$ for demonstration. In Figure 3a, we present the mean-square displacement (MSD), $g_1(t) = \langle \Delta r^2(t) \rangle$, where $\Delta r(t)$ is the particle displacement at time t, of neutral beads at different T. The MSD curve initially

exhibits a ballistic motion at small t, with $g_1(t) \propto t^2$, for polymer beads moving within the 'cage' formed by neighboring beads. At high temperatures, MSD enters into a sub-diffusive regime dictated by the Rouse-like motion of the polymer chain (ideally, $g_1(t) \propto t^{0.5}$) after decaging and before transitioning to a diffusive regime (where $g_1(t) \propto t$, not reached in the probed time window). As T is decreased, the cage size and corresponding $g_1(t)$ in the ballistic regime reduce in magnitude under the contraction of system size. Meanwhile, losing thermal energy weakens the capability of bead reconfiguration, extending the decaging process. This develops a plateau in MSD between ballistic and sub-diffusive regimes approaching T_g (e.g., $T = 0.45$). For systems below T_g, the plateau regime significantly enlarges, which is characteristic of the glassy state.

In Figure 3b, we plot the non-Gaussian parameter, $\alpha_2(t) = (3/5)\langle \Delta r^4(t) \rangle / \langle \Delta r^2(t) \rangle^2 - 1$, at different T, which quantifies the deviation of the monomer motion from random diffusion exhibiting a Gaussian distribution in the displacement. The larger α_2, the greater the dynamic heterogeneity in the system. At high temperatures, the primary peak position t^* corresponds to the middle of the crossover from ballistic to sub-diffusive regimes,[57] and its primary peak height, $\alpha_2(t^*)$, is relatively small. Along with decreasing T, the peak magnitude increases and the peak position shifts towards larger t. Significant increases in t^* and $\alpha_2(t^*)$ emerge upon approaching T_g (e.g., $T = 0.45$); further increases are observed for $T < T_g$, indicating the persistence of larger dynamic heterogeneities for longer timescales which implies the collective motion[31] of polymer beads in the glassy state.

We employ the bond orientation autocorrelation function, $P_2(t) = \langle 3[\mathbf{b}_i(0) \cdot \mathbf{b}_i(t)]^2 - 1 \rangle / 2$ where $\mathbf{b}_i(t)$ is the i-th bond orientation unit vector at time t, to probe polymer relaxation and segmental dynamics. Figure 3c shows the results of $P_2(t)$ with including all polymer bonds at different T. In general, $P_2(t)$ exhibits a two-step decay in the melt of ionic polymers, corresponding to the precursor β-relaxation (related to monomer rearrangement and intrachain motions[58]) and the structural α-relaxation, respectively.[19] At large T, $P_2(t)$ decays fast, on a time scale much shorter than the Rouse time associated with the chain dynamics (cf. Fig-

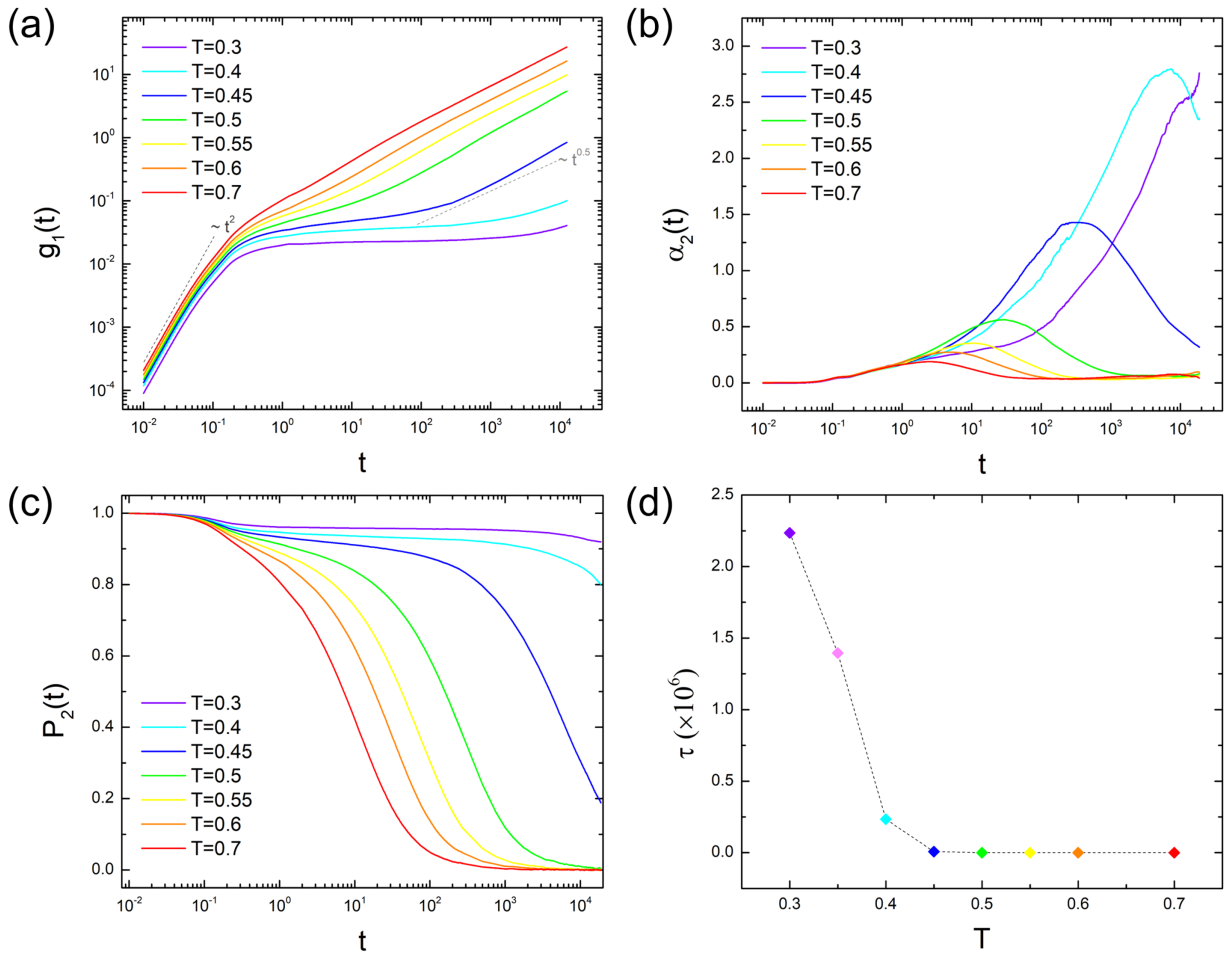

Figure 3: Polymer dynamic properties for bulk random ionic polymers of $f_c = 0.1$ and $l_B = 5.6$: (a) Mean-square displacement $g_1(t)$ of neutral beads at different T. (b) Non-Gaussian parameter $\alpha_2(t)$ of neutral beads at different T. (c) Bond orientational autocorrelation function $P_2(t)$ of ionic polymers at different T. (d) Correlation time τ, extracted from fitting $P_2(t)$ at long time scales (α-relaxation) by a scaled Kohlrausch–Williams–Watts (KWW) function $f(t) = a\exp[-(t/\tau)^\beta]$, as a function of T.

ure S3). Decreasing T elongates the decorrelation process while the change becomes more prominent going through the glass transition. We extract the correlation time of the segmental dynamics, τ, by fitting the α-process to a scaled Kohlrausch–Williams–Watts (KWW) function, $f(t) = a\exp[-(t/\tau)^{\beta}]$. The obtained τ is presented in Figure 3d as a function of T, displaying a manifest jump in magnitude from $T = 0.45$ to 0.4 that passes $T_g \approx 0.424$. This demonstrates that the glass transition kinetically freezes the segmental relaxation of polymer chains.

These dynamic properties capture typical features of polymer glass transition, which are also present in other polymeric systems.[19,57,59] We further inspect the property of ionic aggregates inside the systems and examine its interplay with the glass transition. In Figure 4a, we plot the radial distribution function between ca and ci, $g_{\text{ca-ci}}(r)$, for different l_B in systems of $f_c = 0.1$ and $T = 1.0$. At $l_B = 0$ where charged particles only experience LJ interactions, $g_{\text{ca-ci}}(r)$ displays a liquid-like behavior. With increasing l_B, the primary peak develops, exhibiting a monotonic increase in height along with shifting towards smaller r (Figure S7). Meanwhile, the shape of $g_{\text{ca-ci}}(r)$ at small l_B is similar as $l_B = 0$, which indicates a loose association of charged particles at weak ionic correlations. At large l_B, the ionic association becomes more compact, while long-range orders emerge such that apparent changes in the second and third coordination shells are observed in $g_{\text{ca-ci}}(r)$ from $l_B = 11.2$ to 22.4. This is consistent with previous findings[38] (despite different types of polymer interactions in the models, i.e., attractive versus purely repulsive), suggesting a distinct structural difference between ionic associations at weak and strong ionic correlations.

We perform cluster analysis on the ionic aggregates based on a distance criterion. Specifically, two charged particles within the distance of $d = 1.08$, corresponding to the primary peak position of $g_{\text{ca-ci}}(r)$ in the neutral case in Figure 4a, are designated to belong to the same cluster. As shown in Figure S8, the cluster size, N_c, increases with decreasing T, while the variation in the number of clusters, n_c, along with time reduces as l_B increases and T decreases. In Figure 4b, we present the distribution of N_c for systems of different l_B at

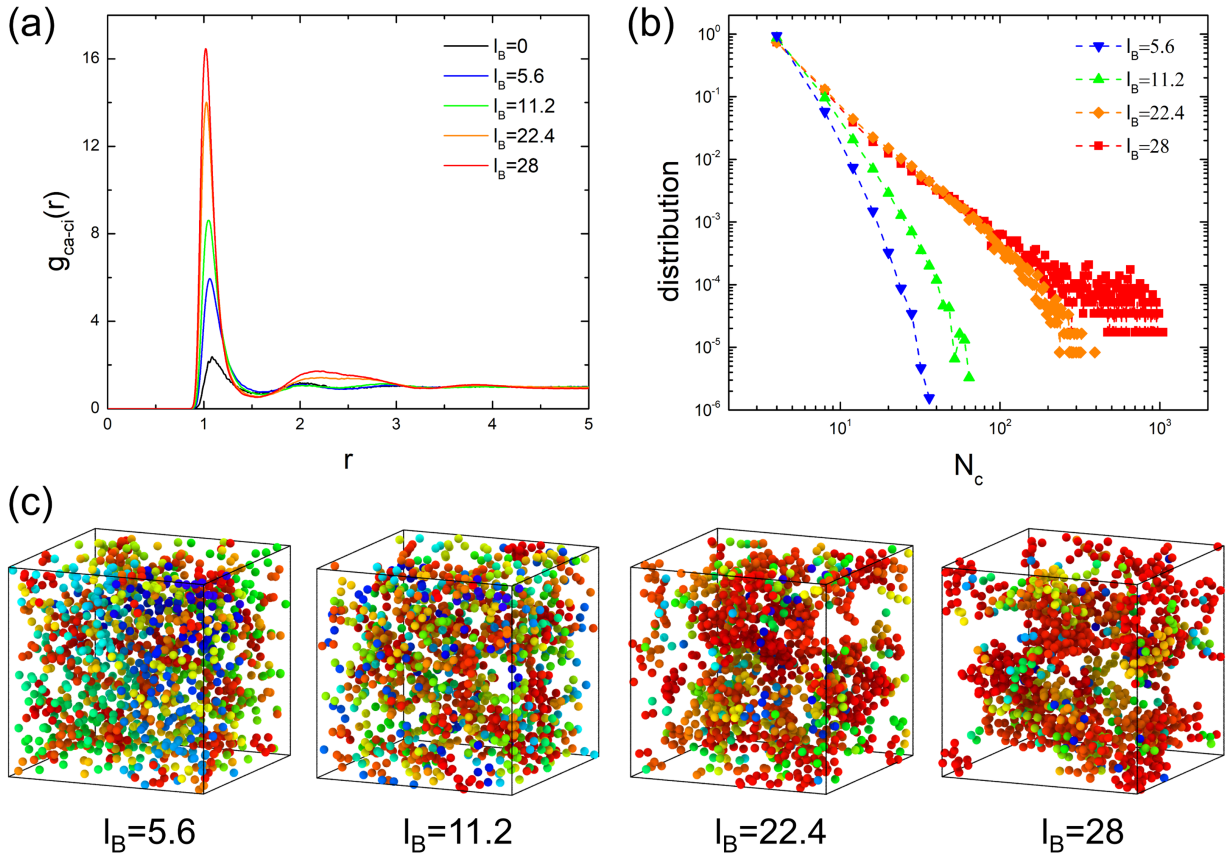

Figure 4: Configurational properties of charged particles in systems of $f_c = 0.1$ and $T = 1.0$: (a) Radial distribution function between charged bead and counterion, $g_{\text{ca-ci}}(r)$, at different l_B. (b) Distribution of ionic cluster size N_c at different l_B. Clusters are determined based on a distance criterion that two particles within a distance of $d = 1.08$ belong to the same cluster. (c) Typical configuration of the ionic association at different l_B, color-coded differently per individual ionic clusters.

$T = 1.0$. Larger l_B leads to the formation of larger clusters. The evident change in the distribution curve from $l_B = 11.2$ to 22.4 corroborates the shape difference of $g_{\text{ca-ci}}(r)$, suggesting a morphological transition of ionic association from discrete to percolating structures[38] with increasing l_B as illustrated in Figure 4c. The change in ionic aggregation structures accordingly modulates the packing and pair correlation between ca and ci, dictating the nonlinear increase in the primary peak of $g_{\text{ca-ci}}(r)$ (Figure S7).

In Figure 5a, we contrast the relaxation of bond orientation for different l_B (at $T = 1.0$). With increasing l_B, the $P_2(t)$ curve shifts towards a larger t, extending the decorrelation process. It indicates that the formed ionic aggregates impose a pinning effect that hinders the polymer relaxation. Such an effect is more significant on the bonds connecting ca and na beads, which induces larger shifts in the associated $P_2(t)$. The corresponding changes are captured by the variation of correlation time τ in Figure 5b. Particularly, τ of ca-na bonds exhibits a monotonic increase with l_B, which is ascribed to the pinning of electrostatic interactions and the steric hindrance due to the effective physical crosslinking by the ionic aggregates. The pinning effect is passed to neutral beads via chain connectivity and causes an increase in τ of na-na bonds. However, its increment is smaller compared to τ of ca-na bonds, and the difference between the two curves increases as l_B is increased. This implies a decoupling in the dynamics of ca and na beads while the increasing electrostatic interaction strength enlarges the dynamic heterogeneity of the system.

The decoupling between the motions of ca and na beads along with increasing the ionic correlations is also exposed by the separation of their MSD profiles in Figure S9. The ca MSD becomes smaller than the na MSD as l_B increases, suggesting that the movement of compact ionic aggregates is slower than neutral beads. The dragging of ionic aggregates in turn, reduces the MSD of na beads at large l_B (Figure S9). Comparatively, smaller polymer MSD, larger dynamic heterogeneity, and slower α-relaxation at the same temperature synergistically signify that the system is closer to the glass transition and hence, has a larger T_g.

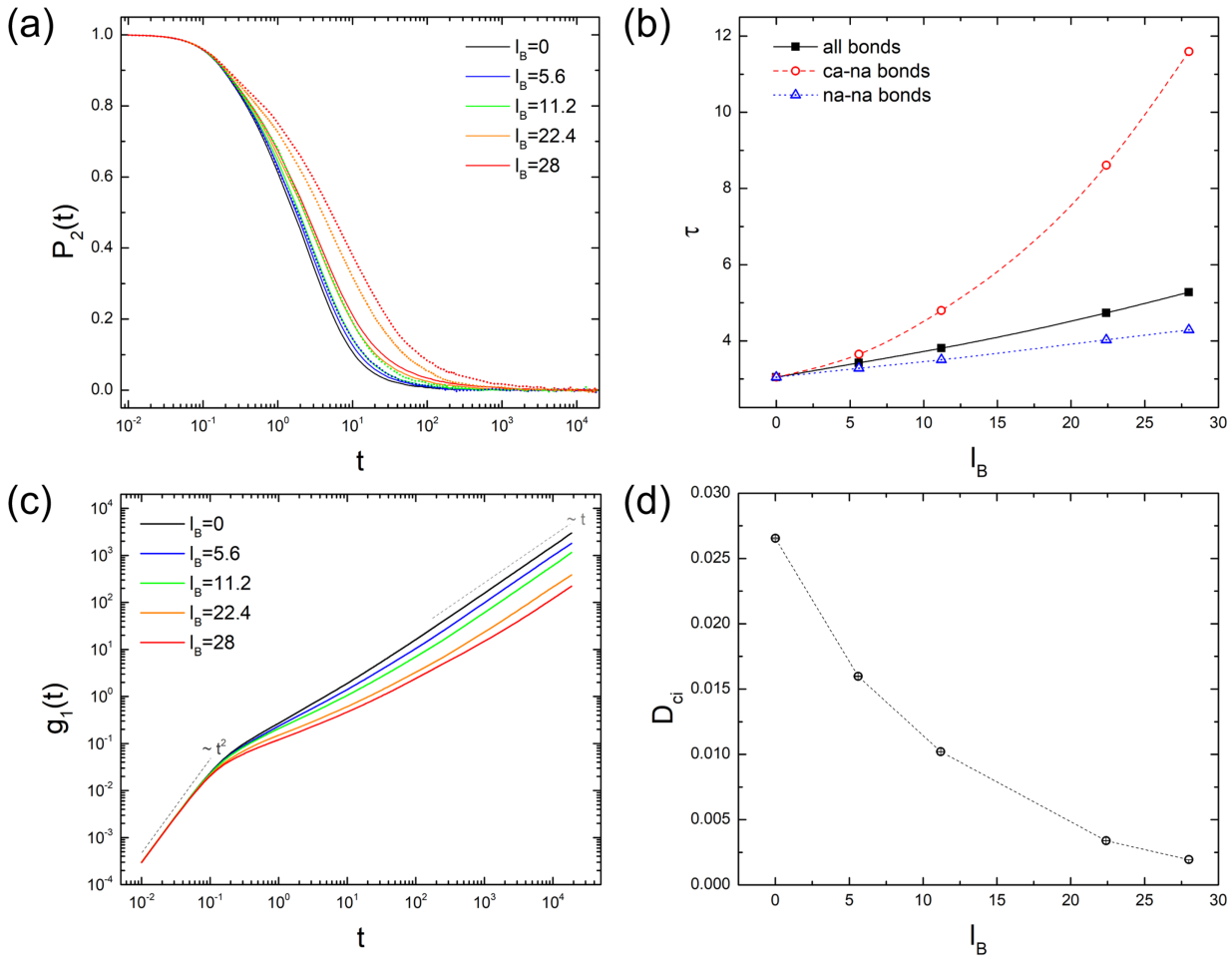

Figure 5: (a) Bond orientational autocorrelation function $P_2(t)$ of random ionic polymers of $f_c = 0.1$ and $T = 1.0$ for different l_B. Solid lines show the results of including all polymer bonds, and dotted lines correspond to bonds connecting ca and na beads. (b) Correlation time τ of α-process in $P_2(t)$ (from KWW fitting) as a function of l_B for different bonds. (c) Mean-square displacement $g_1(t)$ of counterions for different l_B. (d) Diffusion coefficient of counterions, $D_{\rm ci}$, extracted from $g_1(t) = 6Dt$ in the diffusion regime, as a function of l_B.

We further examine the counterion diffusivity in systems of different l_B. The ci MSD profiles at $T = 1.0$ are presented in Figure 5c, showing a ballistic regime at small t and a diffusive regime at large t. The decaging process of ci is shorter at larger l_B. Also, for $l_B \neq 0$, the ci MSD couples with the ca MSD in the intermediate time regime (cf. Figure S9). The duration of the coupling between ci and ca motions increases with increasing l_B, reducing the mobility of ci beads. In consequence, the extracted diffusion coefficient of counterions, D_{ci}, exhibits a monotonic decrease with l_B in Figure 5d, which is in an opposite trend with the variation of ionic correlation (Figure S7). Correspondingly, it appears that the larger T_g of ionic polymers, the smaller the counterion mobility (and the lower the ionic conductivity) inside the system at ambient temperature (Figure S10), consistent with experimental findings.[60]

Effect of the charge fraction. Next, we inspect the effect of charge fraction f_c on the glass transition of random ionic polymers. In Figure 6a, we plot V^* against T for bulk systems of different f_c at typical l_B for weak and strong ionic correlations, respectively. The larger f_c, the more ci beads in the simulation box (see Figure S11 for snapshots of ionic association configurations). At $l_B = 5.6$, the entropic effect of counterions is dominating under weak electrostatic interactions that the ci bead possesses more free volume compared to polymer beads. Thus, V^* shifts upwards with increasing f_c. By contrast, at $l_B = 22.4$, strong electrostatic interactions suppress the ci free volume while effectively increasing the overall cohesive energy, leading to smaller V^*. The larger f_c, the stronger the effect, such that V^* reduces as f_c is increased at high T, which is opposite to the case of $l_B = 5.6$. However, compact percolating ionic aggregates at $l_B = 22.4$ (Figure S11) serve as a supporting 'skeleton' of the bulk system that has comparatively smaller compressibility than the polymer matrix. This hinders the reduction of V^* at low T, and consequently, the V^* curves show different progressions at low and high temperatures. Though the sequence of V^* curves in the glassy state is the same as that of $l_B = 5.6$, the underlying mechanism is different due to the difference in the ionic association structures.

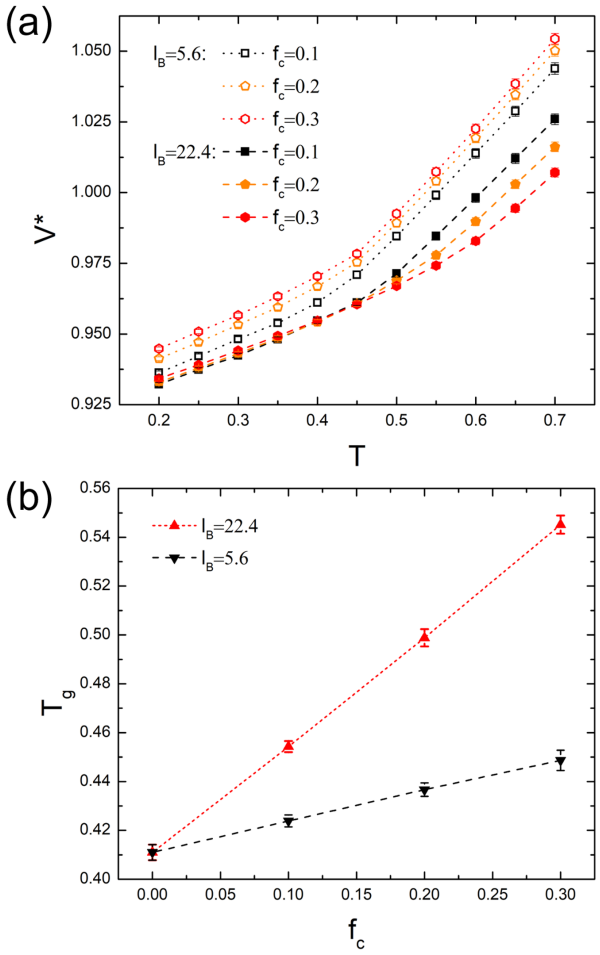

Figure 6: (a) Specific volume V^* as a function of temperature T from cooling (with the cooling rate $\Delta T/\Delta t = -2 \times 10^{-5}\tau^{-1}$) for systems of different f_c at $l_B = 5.6$ and 22.4. (b) Glass transition temperature T_g as a function of f_c, where $f_c = 0$ corresponds to the neat neutral polymer system. The variation of T_g exhibits a linear dependence of f_c, with the slope of 0.126 and 0.447 for $l_B = 5.6$ and 22.4, respectively.

Figure 6b presents T_g as a function of f_c at the two l_B values. Both T_g curves exhibit a linear dependence of f_c with respect to $T_g \approx 0.411$ at $f_c = 0$, corresponding to the associated neat neutral polymer melt. We note that T_g of the neat system is slightly larger than that of $f_c = 0.1$ and $l_B = 0$ where $T_g \approx 0.406$. Although the difference is marginal (and comparable to the error bar), we expect that it is the case, as the 'neutral' ci bead at $l_B = 0$ (with a number fraction of 0.091 at $f_c = 0.1$) works as a plasticizer that lowers the glass transition temperature (as also suggested by the consistent difference in dynamic properties in Figure S12). The linear dependence of T_g on the ion content shows good agreement with experimental findings.[61,62] Moreover, the ratio of the slopes is less than the ratio between l_B, i.e., $0.447/0.126 \approx 3.55 < 4.0$, reminiscent of the sublinear dependence of T_g on l_B shown in Figure 2b. This further implies that the effect of l_B on T_g is general for systems of different f_c and hence, the dependence of T_g on l_B and f_c might be factorized into separate components for the considered systems.

Effect of the charge sequence. We probe the effect of charge sequence by comparing random and precise ionic polymers of the same charge fraction. Figure 7a plots $g_{\text{ca-ci}}(r)$ for two types of ionic polymers with $f_c = 0.1$ and $T = 0.7$ at two typical l_B values (see Figure S13 for corresponding configurations of charged particles). Despite the morphological similarity between ionic associations at different l_B, random ionic polymers show larger primary peaks in $g_{\text{ca-ci}}(r)$ as well as stronger correlations in high order peaks, while the differences are bigger at larger l_B. This is attributed to the difference in the steric shielding by neutral polymer segments that the chain connectivity interrupts the packing of charged particles in the coordination shells.[43] The irregular contour spacing between charged beads of the random sequence allows more combinations for packing of charged particles that alleviates the steric constraint for ion pairing, leading to a larger ionic correlation compared to the precise case.

Accordingly, the larger ionic correlation enlarges the cohesive energy of the system more and causes larger dynamic heterogeneity, as demonstrated by the comparisons of nearest-

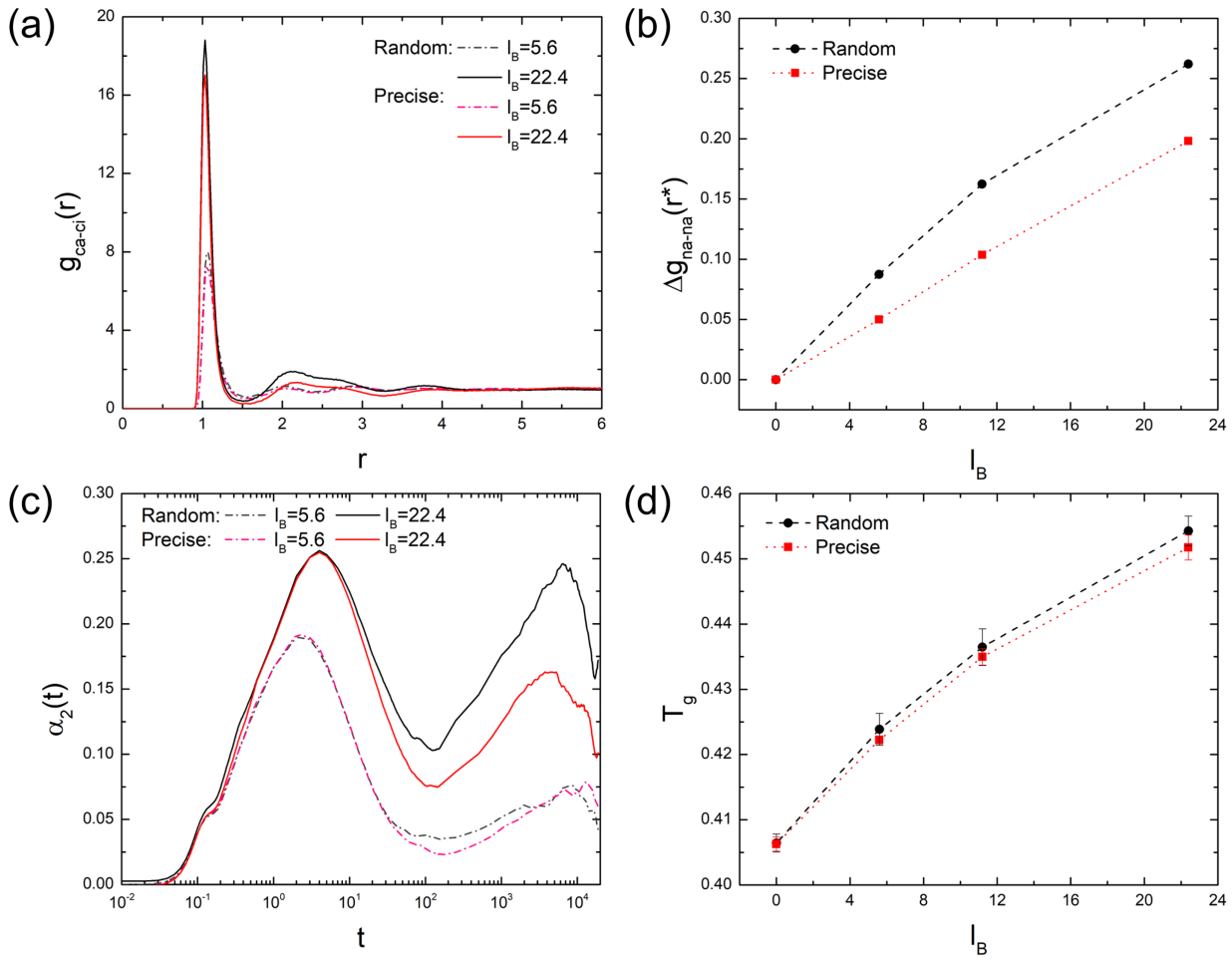

Figure 7: Comparison between random and precise charge sequences with the same total charge fraction $f_c = 0.1$ at $T = 0.7$ and different l_B: (a) Radial distribution function between charged bead and counterion, $g_{\text{ca-ci}}(r)$; (b) relative height of the nearest-neighbor peak in $g_{\text{na-na}}(r)$ (with respect to the neutral case) as a function of l_B; and (c) non-Gaussian parameter $\alpha_2(t)$ of neutral beads. (d) Glass transition temperature T_g as a function of l_B.

neighbor peak height in $g_{\text{na-na}}(r)$ and non-Gaussian parameter $\alpha_2(t)$ of neutral beads at $T = 0.7$ in Figure 7b and 7c, respectively (see Figure S14 for the associated difference between $P_2(t)$ of all bonds). These behaviors suggest that random ionic polymers should have relatively greater T_g than the corresponding precise ones. The plots of T_g versus l_B for the two types of charge sequences in Figure 7d support the expectation that the T_g curve of the random sequence is higher than that of the precise sequence, while their difference increases with increasing l_B. Therefore, changing the charge sequence from random to precise lowers the glass transition temperature. In addition, we note that combining charge sequence with complex polymer architectures is worthy of further exploration for modulating T_g by means of steric hindrance on ionic correlations via chain connectivity.

Glass transition in thin films. Lastly, we discuss the behavior of glass transition in thin films of ionic polymers, with a focus on the film thickness effect. To be specific, our model system corresponds to confined films by smooth walls, in contrast to free-standing films, supported films with a free surface, and films confined with rough walls (which have been extensively studied for neutral polymer systems[19,21,63]). Generally, a thin film with sufficient film thickness can be divided into two surface layers and a bulk-like layer, while the surface layers are separated by the bulk-like layer and do not interfere. Ionic polymer thin films share the same character. Figure 8a shows the density profiles of different types of particles for random ionic polymers of $f_c = 0.1$ and $l_B = 5.6$ near the wall in a film of $h = 20$ at $T = 0.7$. The polymer density undergoes a 'healing' process from the wall and then oscillations before recovering the bulk value, which shows a surface-induced ordering and indicates that the surface layer is of $\sim 5\sigma$ thick. The ci density mostly overlays with the ca density under the ionic correlation (see Figure S15 for the comparison with the neutral $l_B = 0$ case). Meanwhile, the ci density is comparatively higher than ca close to the wall due to the entropic effect, as polymer chains have larger entropy loss near the wall. This effect causes a local decoupling between ci and ca densities, while its range is smaller than the size of the surface layer.

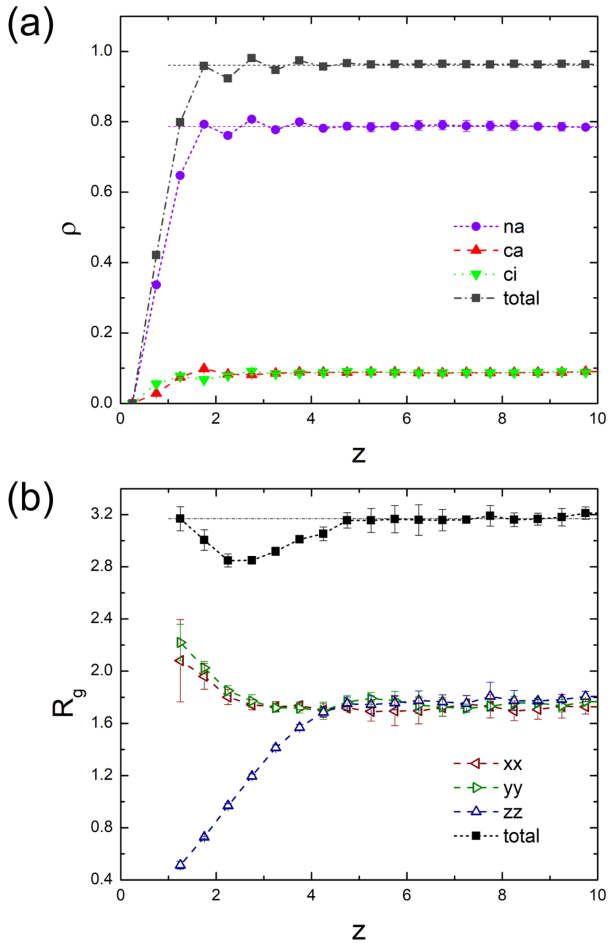

Figure 8: (a) Profiles of number density ρ for different components near the wall in random ionic polymer film of thickness $h = 20$ at $f_c = 0.1$, $l_B = 5.6$, and $T = 0.7$ along the film thickness direction z. Dashed lines indicate average values from the corresponding bulk system. (b) Layer-resolved profile of radius of gyration R_g of ionic polymers, showing tensor elements in all three directions. The dashed line refers to the bulk R_g value.

Figure 8b presents a layer-resolved analysis of ionic polymer size in terms of the radius of gyration, R_g, based on the polymer center-of-mass position in the z-direction. The tensor elements of xx, yy, and zz are also shown to probe the polymer morphology. Specifically, R_g^{xx} and R_g^{yy} exhibit the same behavior according to the lateral symmetry, which decrease in magnitude moving away from the wall and level off in the bulk-like layer. By contrast, R_g^{zz} shows an opposite trend, which starts small at small z, increases with increasing z, and then reaches the plateau with the same value as R_g^{xx} and R_g^{yy}. In consequence, R_g initially decreases and then increases inside the surface layer, showing a non-monotonic variation. This suggests that ionic polymers assume a pancake-like shape near the wall and are spherical in the bulk-like layer. Furthermore, it indicates the recovery of bulk behavior at $z \approx 5$, in accord with the finding from the density profiles (Figure 8a).

We further perform the layer-resolved analysis on dynamic properties inside the film. For $h = 20$, we consider five layers. Each layer is of thickness 2 and indexed by an increasing number moving away from the wall, i.e., layer-1 is at the wall and layer-5 is at the center of the film. In Figure 9, we plot the profiles of lateral mean-square displacement, $g_1^{xy}(t)$, for neutral beads and bond orientational autocorrelation function, $P_2(t)$, for all polymer bonds, respectively, in different layers. Bulk results are also shown for comparison. In the calculations, the layer index is labeled according to the position of each bead or the middle of each bond in the initial state of individual statistical time window t along the simulation trajectory.

The MSD profiles share similar ballistic regimes at small t and exhibit decreasing magnitude from layer-1 to layer-4 in the sub-diffusive regime as the polymer density increases moving inside the film (e.g., the layer-averaged number density of total particles $\bar{\rho} = 0.544$, 0.956, 0.962, 0.964, and 0.964 from layer-1 to layer-5 in Figure 8a). The curves of layer-4 and layer-5 are about the same and overlay with the bulk result. The same trend is observed in the $P_2(t)$ plots. It shows the fastest decay in layer-1, while the polymer relaxation slows down as the layer index increases and recovers the bulk behavior in layer-4. These results

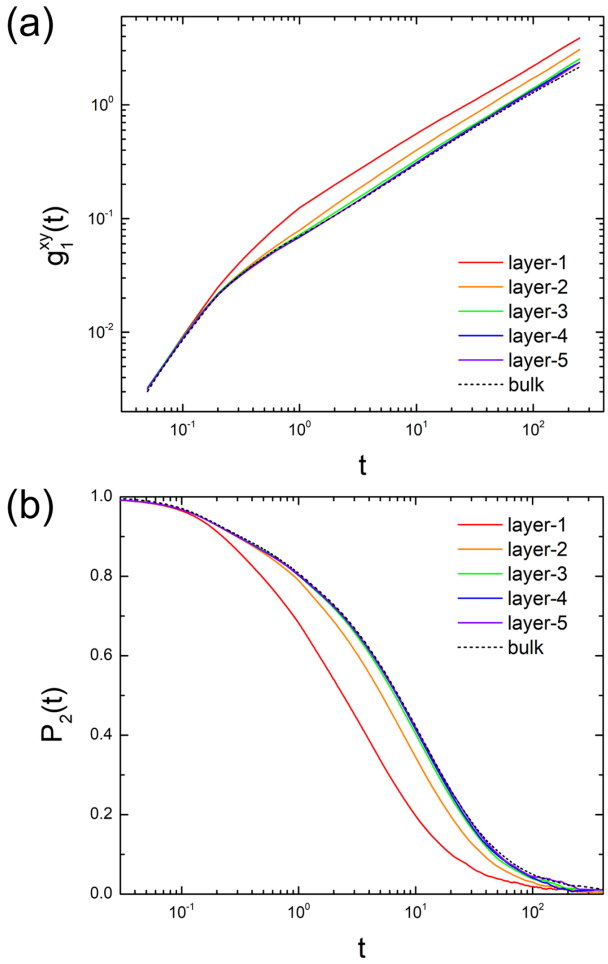

Figure 9: Layer-resolved analysis of dynamic properties in random ionic polymer film of $h = 20$ at $f_c = 0.1$, $l_B = 5.6$, and $T = 0.7$ for (a) lateral mean-square displacement of neutral beads, $g_1^{xy}(t)$, and (b) bond orientational autocorrelation function of polymers, $P_2(t)$, where layer-1 starts at the wall and each layer is of thickness 2. Corresponding bulk results are shown for comparison.

corroborate the assertion of the surface layer size ($d_s \approx 5\sigma$ that the bulk-like layer starts in layer-3) from Figure 8 via density and chain conformation analysis, demonstrating a typical interfacial behavior that ionic polymers have faster dynamics near the surface due to a lower density under the weak surface affinity. This further implies that the surface layer possesses a lower T_g than the bulk-like layer.

Figure 10a plots V^* against T for random ionic polymers of $f_c = 0.1$ and $l_B = 5.6$ in thin films of different thickness h. The shape of the V^* curve in films is similar to the bulk one, exhibiting two linear regimes and a kink in between due to the glass transition. As the films have a lower particle number density (Figure 8a) and hence, a larger V^* in the surface layer compared to the bulk, the average V^* is larger than the bulk value at different T. Also, the V^* curve shifts upwards as h decreases, for the increase of the overall surface layer portion inside the film. In particular, the curve of $h = 6$ shows a drop of V^* at $T = 0.45$, which is caused by the formation of more ordered packing structures (Figure S16) as the relaxation of the system falls onto a crystallization process.[21] By contrast, the other data points on the low-temperature branch of the $h = 6$ curve indicate that those systems are arrested by the glassy state due to the fast cooling in the quenching process. This further suggests that the polymer crystallization can be facilitated in thin films with small h under the same conditions, for which a larger free volume per particle, induced by the interfacial and confinement effects, aids in the particle rearrangement and system equilibration.

In Figure 10b, we present the film-averaged T_g as a function of $1/h$ for systems with different ionic correlations, charge sequences, and interfacial interactions. Particularly, $1/h = 0$ corresponds to the bulk system. The variation of T_g with $1/h$ shows similar behavior in different systems: T_g initially follows an approximately linear decrease with increasing $1/h$ and undergoes a larger decrease at larger $1/h$. The linear dependence at small $1/h$ is rationalized by taking T_g as the summation of contributions from both surface and bulk-like layers. When $h > 2d_s$, the surface layers (symmetric in this model) are dictated by interfacial properties at the wall (such as surface affinity to particles[64]) and are about the same at

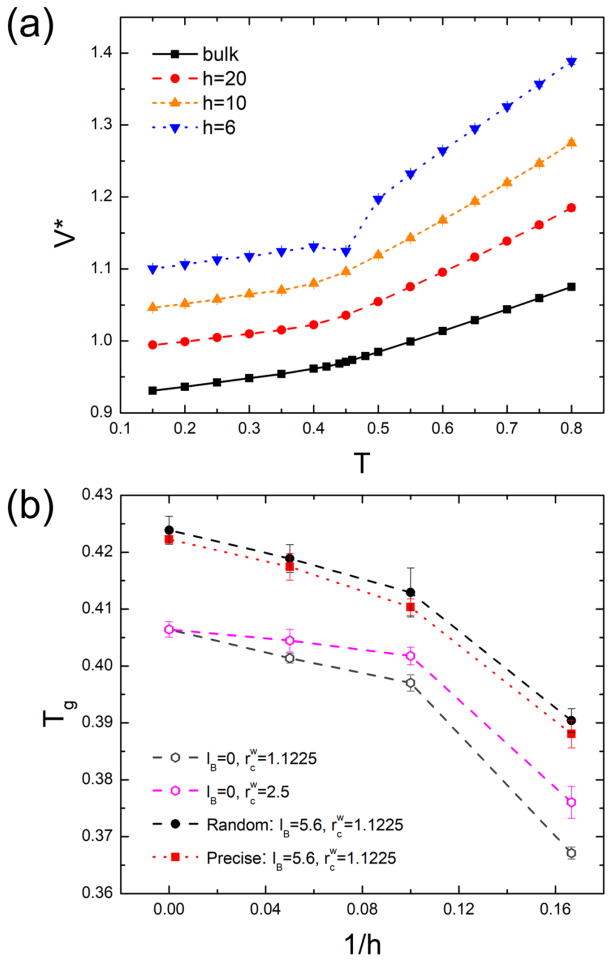

Figure 10: (a) Specific volume V^* as a function of T from cooling (with a constant cooling rate $\Delta T/\Delta t = -2 \times 10^{-5}\tau^{-1}$) in random ionic polymer films of different h at $f_c = 0.1$ and $l_B = 5.6$. (b) T_g as a function of $1/h$ for different wall affinities, electrostatic interaction strengths, and charge sequences.

different h (cf. Figure S17). Therefore, $T_g = 2d_s T_g^s/h + (h-2d_s)T_g^b/h = T_g^b - 2(T_g^b - T_g^s)d_s/h$, where T_g^s is the average glass transition temperature of the surface layer and T_g^b is the bulk glass transition temperature while $T_g^s < T_g^b$ for a lower average density (e.g., $T_g^s \approx 0.413$ and $T_g^b \approx 0.424$ for the random sequence case at $l_B = 5.6$ from the fitting with $d_s \approx 5$). We note that the total number density of particles in the film also exhibits the same linear dependence at large h, as illustrated in Figure S18. The difference between T_g^s and T_g^b suggests a two-step glass transition in films that upon cooling, the vitrification takes place first in the center of the films and then reaches the surfaces.

For $h < 2d_s$, the bulk-like layer vanishes, and two surface layers overlap, leading to a higher density of the confined melt compared to the linear behavior while it decreases with decreasing h (see Figure S18). However, the large decrease in T_g indicates that the glass transition process is different from the one in thicker films, which is connected to the bulk behavior. We attribute the difference to a change in effective cooling. Although the cooling rate is maintained the same in simulations, the increase in V^* results in a larger travel time of particles in the mean free path. Its effect is similar to the reduction in the magnitude of the cooling rate, while a smaller cooling rate causes a lower T_g.[54] Also, the effectively slower cooling facilitates the polymer crystallization that supports the finding at $h = 6$ in Figure 10a.

From contrasting different systems in Figure 10b, one finds that the presented features of ionic polymer glass transition in films are the same as in the bulk. The introduction of ionic correlation enlarges T_g, and changing the charge sequence from precise to random enhances the ionic correlation that further increases T_g. Moreover, we briefly consider the effect of surface affinity by comparing two neutral systems (i.e., $l_B = 0$) with different interaction ranges of wall potentials. Specifically, increasing the cut-off distance from $r_c^w = 1.1225$ to 2.5 increases the attraction well depth from 0.394ϵ to 0.990ϵ, enhancing the wall affinity with particles. This enlarges the particle density near the wall (cf. Figure S19) and slows down the interfacial dynamics, leading to a higher T_g^s and hence, a shallower slope in the initial linear

decrease of T_g with decreasing h. Following this trend, T_g^s could eventually become larger than T_g^b with increasing the wall affinity and surface adsorption, which reverses the sign of the slope, i.e., the film-averaged T_g appears to increase as h is decreased.[55,64] We expect that this effect holds in the case of $l_B \neq 0$, while the detailed coupling of ionic correlations with polymer surface excess requires a further investigation. Herein, our findings suggest that to achieve a lower glass transition temperature of ionic polymers, one could adopt a precise charge sequence, strong confinement, and small surface affinity.

Conclusions

In summary, we have adopted a simplified coarse-grained model and employed systematic molecular dynamics simulations to investigate the glass transition of ionic polymers. We considered the effects of ionic correlation strength, charge fraction, and charge sequence on the glass transition temperature T_g through configurational and dynamical properties. Our study demonstrated that T_g exhibits a sublinear monotonic increase with increasing the strength of electrostatic interactions and ionic correlation characterized by the Bjerrum length l_B, a linear increase with increasing the charge fraction f_c, and a comparatively higher magnitude for the random charge sequence due to the larger ionic correlation. The relative increase in T_g is consistent with the reduction of polymer mean-square displacement, the enhancement of dynamic heterogeneity (as captured by the non-Gaussian parameter), and the slowing down of polymer relaxation in the system. Moreover, the coupling of ionic aggregates with the glass transition is explored, revealing the effects of ionic cluster structures on the ionic correlation and counterion diffusivity. These findings show good agreement with experimental results while providing a detailed molecular insight into the glass transition.

We inspected the interfacial and confinement effects on the glass transition of ionic polymers in thin films confined by smooth walls, with varying film thickness h in different control groups. We showed that the film of sufficiently large thickness consists of two surface lay-

ers and a bulk-like layer in between. The surface layer behavior is dictated by interfacial properties and is about the same in thick films. This accounts for the linear dependence of film-averaged quantities with respect to $1/h$ at large h, such as the total particle number density and T_g, as illustrated by the simulation results. Meanwhile, due to the lower density near the interface (with weak affinity to particles), the surface layer is more mobile, leading to a lower glass transition temperature compared to the bulk. This addresses the reduction of T_g with decreasing h as the overall portion of surface layers in the film increases. Furthermore, a large drop in T_g is observed at small h where the bulk-like layer vanishes and surface layers overlap with each other. The deviation from the linear decrease is attributed to the decrease in the effective cooling rate. The increase of particle free volume under strong confinement enlarges the travel time in the mean free path for particles, resulting in an effectively slower cooling which yields a lower T_g and facilitates the crystallization under the same environmental conditions.

The film thickness effect on T_g is found general for the examined film systems, while its interplay with other features of ionic polymer glass transition displayed in the bulk systems governs the behavior of T_g in films. Overall, our investigation exposed a few typical characters of the glass transition in ionic polymers, suggesting strategies for lowering T_g. We expect that the obtained results have useful implications for understanding the glass transition process as well as designing relevant ion-containing polymeric materials. Lastly, the current minimal model can be readily extended to discern the effects of free ion size, complex polymer architecture, and chain rigidity, etc. Further exploration of the parameter space, as well as the combined effects of different control variables, will offer a more comprehensive understanding of modulating T_g and the coupling of ion transport with polymer dynamics that benefit the rational design of ionic polymers for optimal performance.

Acknowledgement

This work was supported by the U.S. Department of Commerce, National Institute of Standards and Technology as part of the Center for Hierarchical Materials Design (CHiMaD) under award no. 70NANB19H005. The computational resources were provided by the Sherman Fairchild Foundation.

References

(1) Williams, S. R.; Long, T. E. Recent advances in the synthesis and structure–property relationships of ammonium ionenes. *Progress in Polymer Science* **2009**, *34*, 762–782.

(2) Bara, J. E.; O'Harra, K. E. Recent Advances in the Design of Ionenes: Toward Convergence with High-Performance Polymers. *Macromolecular Chemistry and Physics* **2019**, *220*, 1900078.

(3) Grady, B. P. Review and critical analysis of the morphology of random ionomers across many length scales. *Polymer Engineering & Science* **2008**, *48*, 1029–1051.

(4) Seitz, M. E.; Chan, C. D.; Opper, K. L.; Baughman, T. W.; Wagener, K. B.; Winey, K. I. Nanoscale morphology in precisely sequenced poly (ethylene-co-acrylic acid) zinc ionomers. *Journal of the American Chemical Society* **2010**, *132*, 8165–8174.

(5) Zhang, L.; Brostowitz, N. R.; Cavicchi, K. A.; Weiss, R. Perspective: Ionomer research and applications. *Macromolecular Reaction Engineering* **2014**, *8*, 81–99.

(6) Hara, M. *Polyelectrolytes: science and technology*; CRC Press, 1992.

(7) Hallinan Jr, D. T.; Balsara, N. P. Polymer electrolytes. *Annual Review of Materials Research* **2013**, *43*, 503–525.

(8) Mecerreyes, D. Polymeric ionic liquids: Broadening the properties and applications of polyelectrolytes. *Progress in Polymer Science* **2011**, *36*, 1629–1648.

(9) Eftekhari, A.; Saito, T. Synthesis and properties of polymerized ionic liquids. *European Polymer Journal* **2017**, *90*, 245–272.

(10) Middleton, L. R.; Winey, K. I. Nanoscale aggregation in acid-and ion-containing polymers. *Annual Review of Chemical and Biomolecular Engineering* **2017**, *8*, 499–523.

(11) Holdcroft, S. Fuel cell catalyst layers: a polymer science perspective. *Chemistry of Materials* **2014**, *26*, 381–393.

(12) Lewis, C. L.; Dell, E. M. A review of shape memory polymers bearing reversible binding groups. *Journal of Polymer Science Part B: Polymer Physics* **2016**, *54*, 1340–1364.

(13) Cowan, M. G.; Gin, D. L.; Noble, R. D. Poly (ionic liquid)/ionic liquid ion-gels with high "free" ionic liquid content: platform membrane materials for CO2/light gas separations. *Accounts of Chemical Research* **2016**, *49*, 724–732.

(14) Mittenthal, M. S.; Flowers, B. S.; Bara, J. E.; Whitley, J. W.; Spear, S. K.; Roveda, J. D.; Wallace, D. A.; Shannon, M. S.; Holler, R.; Martens, R.; Daly, D. T. Ionic Polyimides: Hybrid Polymer Architectures and Composites with Ionic Liquids for Advanced Gas Separation Membranes. *Industrial & Engineering Chemistry Research* **2017**, *56*, 5055–5069.

(15) Meka, V. S.; Sing, M. K.; Pichika, M. R.; Nali, S. R.; Kolapalli, V. R.; Kesharwani, P. A comprehensive review on polyelectrolyte complexes. *Drug Discovery Today* **2017**, *22*, 1697–1706.

(16) Bagheri, H.; Mohebbi, A.; Jayhani, Z.; Naderi, M. *Advanced Antimicrobial Materials and Applications*; Springer, 2021; pp 87–126.

(17) Lopez, J.; Mackanic, D. G.; Cui, Y.; Bao, Z. Designing polymers for advanced battery chemistries. *Nature Reviews Materials* **2019**, *4*, 312–330.

(18) Ganesan, V. Ion transport in polymeric ionic liquids: recent developments and open questions. *Molecular Systems Design & Engineering* **2019**, *4*, 280–293.

(19) Binder, K.; Baschnagel, J.; Paul, W. Glass transition of polymer melts: test of theoretical concepts by computer simulation. *Progress in Polymer Science* **2003**, *28*, 115–172.

(20) Haward, R. N. *The physics of glassy polymers*; Springer Science & Business Media, 2012.

(21) Napolitano, S.; Glynos, E.; Tito, N. B. Glass transition of polymers in bulk, confined geometries, and near interfaces. *Reports on Progress in Physics* **2017**, *80*, 036602.

(22) Son, C. Y.; Wang, Z.-G. Ion transport in small-molecule and polymer electrolytes. *The Journal of Chemical Physics* **2020**, *153*, 100903.

(23) Schweizer, K. S.; Simmons, D. S. Progress towards a phenomenological picture and theoretical understanding of glassy dynamics and vitrification near interfaces and under nanoconfinement. *The Journal of Chemical Physics* **2019**, *151*, 240901.

(24) Fryer, D. S.; Nealey, P. F.; de Pablo, J. J. Thermal probe measurements of the glass transition temperature for ultrathin polymer films as a function of thickness. *Macromolecules* **2000**, *33*, 6439–6447.

(25) Ediger, M.; Forrest, J. Dynamics near free surfaces and the glass transition in thin polymer films: A view to the future. *Macromolecules* **2014**, *47*, 471–478.

(26) Dudowicz, J.; Freed, K. F.; Douglas, J. F. The glass transition temperature of polymer melts. *The Journal of Physical Chemistry B* **2005**, *109*, 21285–21292.

(27) Lipson, J. E.; Milner, S. T. Local and average glass transitions in polymer thin films. *Macromolecules* **2010**, *43*, 9874–9880.

(28) Baschnagel, J.; Varnik, F. Computer simulations of supercooled polymer melts in the bulk and in confined geometry. *Journal of Physics: Condensed Matter* **2005**, *17*, R851.

(29) Barrat, J.-L.; Baschnagel, J.; Lyulin, A. Molecular dynamics simulations of glassy polymers. *Soft Matter* **2010**, *6*, 3430–3446.

(30) Hung, J.-H.; Patra, T. K.; Meenakshisundaram, V.; Mangalara, J. H.; Simmons, D. S. Universal localization transition accompanying glass formation: Insights from efficient molecular dynamics simulations of diverse supercooled liquids. *Soft Matter* **2019**, *15*, 1223–1242.

(31) Xu, W.-S.; Douglas, J. F.; Sun, Z.-Y. Polymer Glass Formation: Role of Activation Free Energy, Configurational Entropy, and Collective Motion. *Macromolecules* **2021**, *54*, 3001–3033.

(32) Shen, K.-H.; Fan, M.; Hall, L. M. Molecular Dynamics Simulations of Ion-Containing Polymers Using Generic Coarse-Grained Models. *Macromolecules* **2021**, *54*, 2031–2052.

(33) Goswami, M.; Kumar, S. K.; Bhattacharya, A.; Douglas, J. F. Computer simulations of ionomer self-assembly and dynamics. *Macromolecules* **2007**, *40*, 4113–4118.

(34) Hall, L. M.; Stevens, M. J.; Frischknecht, A. L. Effect of polymer architecture and ionic aggregation on the scattering peak in model ionomers. *Physical Review Letters* **2011**, *106*, 127801.

(35) Hall, L. M.; Seitz, M. E.; Winey, K. I.; Opper, K. L.; Wagener, K. B.; Stevens, M. J.; Frischknecht, A. L. Ionic aggregate structure in ionomer melts: Effect of molecular architecture on aggregates and the ionomer peak. *Journal of the American Chemical Society* **2012**, *134*, 574–587.

(36) Hall, L. M.; Stevens, M. J.; Frischknecht, A. L. Dynamics of model ionomer melts of various architectures. *Macromolecules* **2012**, *45*, 8097–8108.

(37) Ting, C. L.; Stevens, M. J.; Frischknecht, A. L. Structure and dynamics of coarse-grained ionomer melts in an external electric field. *Macromolecules* **2015**, *48*, 809–818.

(38) Ma, B.; Nguyen, T. D.; Pryamitsyn, V. A.; Olvera de la Cruz, M. Ionic correlations in random ionomers. *ACS Nano* **2018**, *12*, 2311–2318.

(39) Cheng, Y.; Yang, J.; Hung, J.-H.; Patra, T. K.; Simmons, D. S. Design rules for highly conductive polymeric ionic liquids from molecular dynamics simulations. *Macromolecules* **2018**, *51*, 6630–6644.

(40) Wheatle, B. K.; Lynd, N. A.; Ganesan, V. Effect of polymer polarity on ion transport: a competition between ion aggregation and polymer segmental dynamics. *ACS Macro Letters* **2018**, *7*, 1149–1154.

(41) Dugger, J. W.; Li, W.; Chen, M.; Long, T. E.; Welbourn, R. J.; Skoda, M. W.; Browning, J. F.; Kumar, R.; Lokitz, B. S. Nanoscale resolution of electric-field induced motion in ionic diblock copolymer thin films. *ACS Applied Materials & Interfaces* **2018**, *10*, 32678–32687.

(42) Ma, B.; Nguyen, T. D.; Olvera de la Cruz, M. Control of ionic mobility via charge size asymmetry in random ionomers. *Nano Letters* **2019**, *20*, 43–49.

(43) Li, W.; Carrillo, J.-M. Y.; Sumpter, B. G.; Kumar, R. Modulating Microphase Separation of Lamellae-Forming Diblock Copolymers via Ionic Junctions. *ACS Macro Letters* **2020**, *9*, 1667–1673.

(44) Wong, C.; Clarke, J. H. Molecular dynamics simulation of microstructure and counterion transport in dry ionic heteropolymers. *The Journal of Chemical Physics* **2002**, *116*, 6795–6802.

(45) Ruan, D.; Simmons, D. S. Glass formation near covalently grafted interfaces: Ionomers as a model case. *Macromolecules* **2015**, *48*, 2313–2323.

(46) Ruan, D.; Simmons, D. S. Roles of chain stiffness and segmental rattling in ionomer

glass formation. *Journal of Polymer Science Part B: Polymer Physics* **2015**, *53*, 1458–1469.

(47) Fu, Y.; Bocharova, V.; Ma, M.; Sokolov, A. P.; Sumpter, B. G.; Kumar, R. Effects of counterion size and backbone rigidity on the dynamics of ionic polymer melts and glasses. *Physical Chemistry Chemical Physics* **2017**, *19*, 27442–27451.

(48) Mangalara, J. H.; Mackura, M. E.; Marvin, M. D.; Simmons, D. S. The relationship between dynamic and pseudo-thermodynamic measures of the glass transition temperature in nanostructured materials. *The Journal of Chemical Physics* **2017**, *146*, 203316.

(49) Chremos, A.; Douglas, J. F. Communication: When does a branched polymer become a particle? *The Journal of Chemical Physics* **2015**, *143*, 111104.

(50) Kremer, K.; Grest, G. S. Dynamics of entangled linear polymer melts: A molecular-dynamics simulation. *The Journal of Chemical Physics* **1990**, *92*, 5057–5086.

(51) Li, S.-J.; Xie, S.-J.; Li, Y.-C.; Qian, H.-J.; Lu, Z.-Y. Influence of molecular-weight polydispersity on the glass transition of polymers. *Physical Review E* **2016**, *93*, 012613.

(52) Plimpton, S. Fast parallel algorithms for short-range molecular dynamics. *Journal of Computational Physics* **1995**, *117*, 1–19.

(53) Yeh, I.-C.; Berkowitz, M. L. Ewald summation for systems with slab geometry. *The Journal of Chemical Physics* **1999**, *111*, 3155–3162.

(54) Buchholz, J.; Paul, W.; Varnik, F.; Binder, K. Cooling rate dependence of the glass transition temperature of polymer melts: Molecular dynamics study. *The Journal of Chemical Physics* **2002**, *117*, 7364–7372.

(55) Priestley, R. D.; Cangialosi, D.; Napolitano, S. On the equivalence between the thermodynamic and dynamic measurements of the glass transition in confined polymers. *Journal of Non-Crystalline Solids* **2015**, *407*, 288–295.

(56) Eisenberg, A. Glass transitions in ionic polymers. *Macromolecules* **1971**, *4*, 125–128.

(57) Colmenero, J.; Alvarez, F.; Arbe, A. Self-motion and the α relaxation in a simulated glass-forming polymer: Crossover from Gaussian to non-Gaussian dynamic behavior. *Physical Review E* **2002**, *65*, 041804.

(58) Arbe, A.; Richter, D.; Colmenero, J.; Farago, B. Merging of the α and β relaxations in polybutadiene: A neutron spin echo and dielectric study. *Physical Review E* **1996**, *54*, 3853.

(59) Li, S.-J.; Qian, H.-J.; Lu, Z.-Y. A simulation study on the glass transition behavior and relevant segmental dynamics in free-standing polymer nanocomposite films. *Soft Matter* **2019**, *15*, 4476–4485.

(60) Stacy, E. W.; Gainaru, C. P.; Gobet, M.; Wojnarowska, Z.; Bocharova, V.; Greenbaum, S. G.; Sokolov, A. P. Fundamental limitations of ionic conductivity in polymerized ionic liquids. *Macromolecules* **2018**, *51*, 8637–8645.

(61) Ma, X.; Sauer, J.; Hara, M. Poly (methyl methacrylate) based ionomers. 1. Dynamic mechanical properties and morphology. *Macromolecules* **1995**, *28*, 3953–3962.

(62) Kim, S.-H.; Kim, J.-S. Relationships between the glass transition temperatures and the type of cations in poly (ethyl acrylate) ionomers. *Macromolecules* **2003**, *36*, 2382–2386.

(63) Hanakata, P. Z.; Pazmiño Betancourt, B. A.; Douglas, J. F.; Starr, F. W. A unifying framework to quantify the effects of substrate interactions, stiffness, and roughness on the dynamics of thin supported polymer films. *The Journal of Chemical Physics* **2015**, *142*, 234907.

(64) Napolitano, S. Irreversible adsorption of polymer melts and nanoconfinement effects. *Soft Matter* **2020**, *16*, 5348–5365.

Graphical TOC Entry